

Volatile Organic Compound Detection Using Insect Odorant-Receptor Functionalised Field-Effect Transistors

by

Eddyn Oswald Perkins Treacher

A thesis submitted in fulfilment of the
requirements of the degree of
Doctor of Philosophy in Physics
School of Physical and Chemical Sciences
Te Herenga Waka - Victoria University of Wellington

Sep 2023



Acknowledgements

69450

Rifat, Alex - vapour sensor
Erica Cassie - FET sensing setup
Rob Keyzers and Jennie Ramirez-Garcia - NMR spectra
Patricia Hunt - Computational chemistry

1. Characteristics of Pristine Carbon Nanotube & Graphene Field Effect Transistors

103704

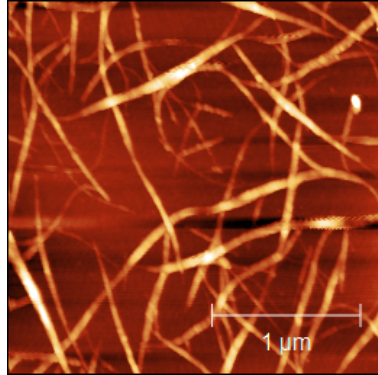
1.1. Carbon Nanotube Network Morphology

Figure 1.1 shows a side-by-side comparison of the surface morphology of carbon nanotube films fabricated using the methods described in [?@sec-dep-carbon-nanotubes](#). These images were collected using an atomic force microscope and processed in the manner described in [?@sec-afm-characterisation](#). They each show bundles of carbon nanotubes with a range of diameters and lengths, with each bundle containing one or multiple nanotubes. As discussed in previous works using solvent-based deposition techniques for depositing carbon nanotubes, multi-tube bundles form due to strong mutual attraction between nanotubes [1]–[4]. However, when surfactants are present, they adsorb onto the carbon nanotubes and form a highly repulsive structure able to overcome the strong attraction between nanotubes. This repulsion then keeps the individual carbon nanotubes isolated [5], [6]. The diameter range provided by the supplier for the individual carbon nanotubes used is 1.2 – 1.7 nm, while the length range is 0.3 – 5.0 μm (Nanointegris).

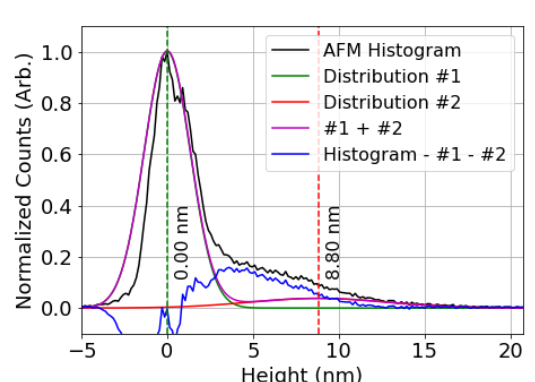
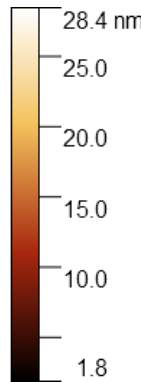
The diameter range of deposited single-walled carbon nanotubes can be modelled via a normal or Gaussian distribution [2], [7], [8]. However, when we extract and bin the height profiles from the $2.5 \mu\text{m} \times 2.5 \mu\text{m}$ AFM images, plotted in black in Figure 1.1, the histograms do not follow a normal distribution. The reason for this result is that the carbon nanotubes do not lie perfectly level on a perfectly level silicon oxide substrate - the atomic force microscope histogram would only be a single normal distribution in this ideal case. In practice, the SiO_2 substrate and carbon nanotube surface both have a degree of roughness, which may in part be due to the presence of atmospheric contaminants. In the case of the surfactant-deposited networks, residual surfactant may also contribute to surface roughness [8]. Furthermore, nanotubes overlap and cross over each other, creating junctions with the combined height of the overlapping nanotubes.

It has been demonstrated that the surface roughness of a bare SiO_2 substrate can also be modelled with a normal distribution. This normal distribution can be set as the reference

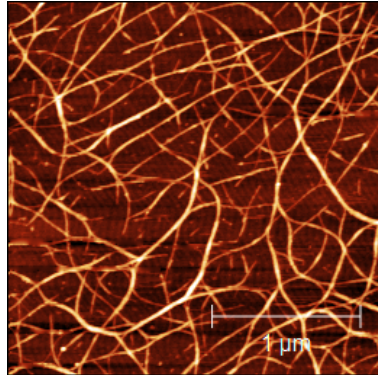
1. Characteristics of Pristine Carbon Nanotube & Graphene Field Effect Transistors



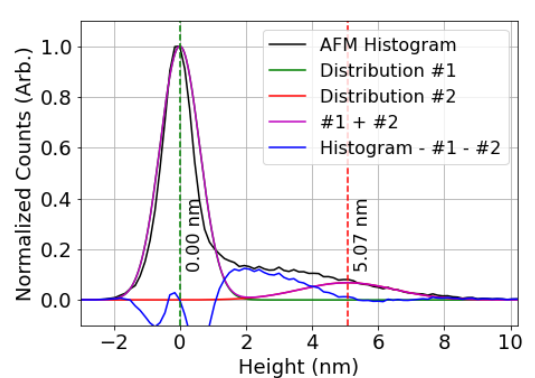
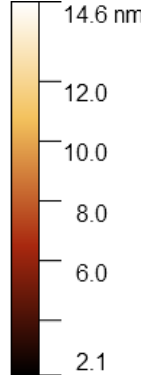
(a) Solvent-based deposition



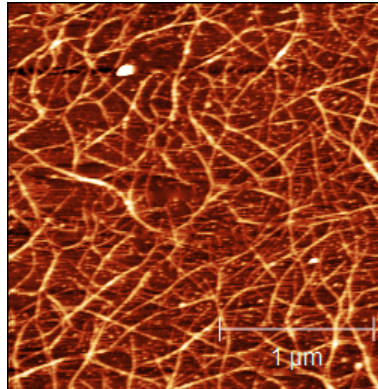
(b) Solvent based deposition histogram



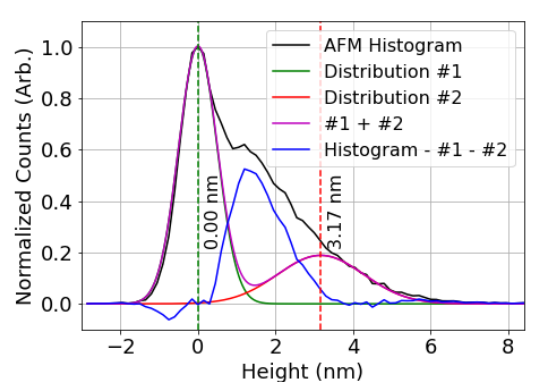
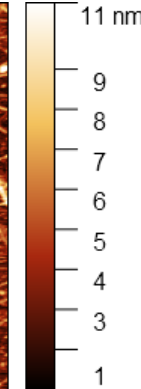
(c) Dropcast surfactant-based deposition



(d) Dropcast surfactant-based deposition histogram



(e) Steam-assisted dropcast surfactant-based deposition



(f) Steam-assisted dropcast surfactant-based deposition

Figure 1.1.: $2.5 \mu\text{m} \times 2.5 \mu\text{m}$ atomic force microscope (AFM) images of carbon nanotube films deposited using various methods, shown side-by-side with surface profile histograms extracted from the AFM profile. Each histogram is shown alongside a linear combination of normal distributions #1 and #2, corresponding to the silicon and carbon nanotube distribution respectively. The counts remaining after #1 and #2 have been subtracted from the AFM histogram are shown in blue.

1.1. Carbon Nanotube Network Morphology

or zero point for other height measurements [9]. As both the carbon nanotube and silicon dioxide background heights can each be modelled using a normal distribution, we make an initial assumption that a linear combination of normal distributions can be used to model the AFM histograms in Figure 1.1. Using the process discussed in Section B.2, we approximate the normal distributions corresponding to the silicon oxide substrate and carbon nanotube network, shown in Figure 1.1 as green and red curves respectively. The silicon oxide peak appears to fit more closely to the distribution with smaller carbon nanotube heights, which could be due to measurement of the silicon background being improved when feature height is smaller. We notice that the distribution for the carbon nanotube bundles drops to approximately zero before reaching 0 nm, which is physically appropriate.

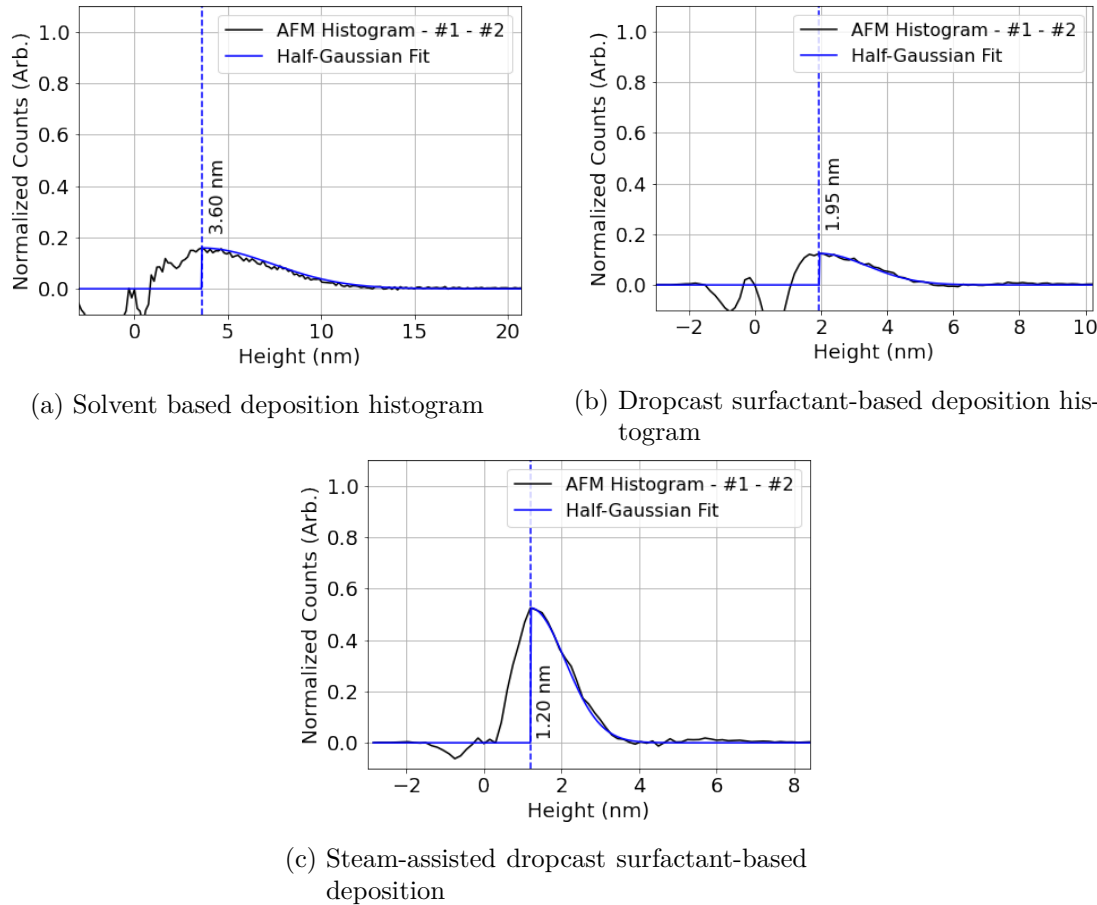


Figure 1.2.: The counts which remain after #1 and #2 have been subtracted from the AFM histogram are shown in black. The counts have been overlaid with half a Gaussian distribution, manually fitted.

By subtracting the modelled silicon and carbon nanotube normal distributions from the AFM histogram, we find a remaining distribution spread roughly between 0 nm and the

1. Characteristics of Pristine Carbon Nanotube & Graphene Field Effect Transistors

mean of the carbon nanotube bundle distribution. Interestingly, the peak of the carbon nanotube distribution occurs at a height approximately $2.5 \times$ the height corresponding to the peak of the remaining distribution. It is also apparent that the remaining distribution consistently follows a normal distribution after a sharp rise to maximum, as shown in Figure 1.2. This distribution appears to correspond to surface roughness due to the presence of contaminants, or possibly to broken pieces of individual nanotubes with various lengths. Contaminants could be residual surfactant or other atmospheric contamination resistant to acetone and isopropanol rinsing. Such contamination may or may not have implications for biosensing suitability, but surfactant contamination could certainly have negative effects on biological elements sensitive to surfactant. The area of this central peak may be useful for determining the extent of contamination on a carbon nanotube film, discussed further in ?@sec-contamination.

If we model carbon nanotube bundles as cylinders, and we assume the component nanotubes follow 2D packing and are of equal diameter, we can give an estimate the mean bundle size for each deposition type in terms of number of nanotubes n [2], [10], [11].

Table 1.1.: The first eight optimised ratios of 2D packed circle diameter to encompassing circle diameter, given to 3 s.f. (encompassing circle diameter = d , number of packed circles = n , approximate packed circle diameter = d_n).

n	2	3	4	5	6	7	8	9
d/d_n	2.00	2.15	2.41	2.70	3.00	3.00	3.30	3.61

Table 1.1 shows the relationship between the diameter of a bundle and the constituent diameters of up to nine 2D packed carbon nanotubes within that bundle. Assuming an average carbon nanotube diameter of 1.45 ± 0.13 nm, we can use the d/d_n packing ratios to obtain an estimate of the number of nanotubes in the mean bundle size for each deposition [11]. These estimates are shown in Table 1.2. Also shown is an estimate of the ratio of single- to multi-tube bundles for each deposition, found by comparing the proportion of each carbon nanotube curve below and above 2.9 nm, the minimum multi-tube bundle size for 1.45 nm diameter nanotubes.

When surfactant is used in the deposition process, both the carbon nanotube bundle diameter mean and standard deviation are small compared to the mean and standard deviation of solvent deposited films. However, despite the presence of surfactant, it is apparent both from Figure 1.1 and Table 1.2 that not all surfactant-dispersed carbon nanotubes are deposited individually. Bundling may occur during the process of deposition onto the substrate, which could disrupt the repulsive forces from the surfactant coating and allow attractive forces to temporarily dominate.

It is possible that the bundling of surfactant-dispersed carbon nanotubes occurs due to the coffee-ring effect [12], [13]. The coffee-ring effect refers to a build-up of dispersed

1.2. Electrical Characteristics

Table 1.2.: The mean of histogram distributions for carbon nanotube films deposited using various methods, along with estimates of the mean number of nanotubes and the proportion of multi-tubed bundles present.

	Distribution Mean (nm)			Bundle Attributes	
	Silicon	Bundles	Contaminant	Mean no. tubes	% multi-tube
Solvent deposited	0.0 ± 1.4	8.8 ± 4.0	3.6 ± 3.8	28 ± 34	~95%
Surfactant deposited	0.0 ± 0.6	5.1 ± 1.4	2.0 ± 1.5	8 ± 7	~94%
Surfactant deposited with steam	0.0 ± 0.5	3.2 ± 1.1	1.2 ± 0.9	3 ± 2	~60%

solid forming around the edges of a dispersion evaporating on a surface. This process occurs due to the dispersion edges being fixed by surface forces, leading to capillary flow outwards to replace liquid evaporating at the edges, bringing solid material along with it. The presence of vapour is known to disrupt this effect [14].

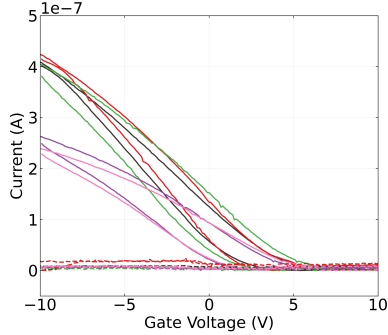
1.2. Electrical Characteristics

1.2.1. Carbon Nanotubes

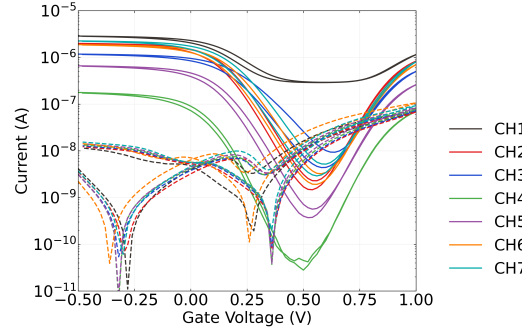
Each carbon nanotube device fabricated was electrically characterised as described in ?@sec-electrical-characterisation. Figure Figure 1.3 displays multi-channel measurements of representative devices fabricated as described in ?@sec-fabrication. To ensure a consistent comparison, each device here was encapsulated with AZ® 1518 encapsulation before measurements were taken. The channels which did not exhibit reliable transistor characteristics are not shown. These ‘non-working’ channels were either shorted, due to metal remaining on the channel after lift-off, or were very low current, due to a very sparse carbon nanotube network. Devices shown here with a solvent-deposited carbon nanotube network were fabricated prior to Jan 2022; devices with a surfactant-deposited network without steam present were fabricated prior to Jun 2021; devices with a surfactant-deposited network without steam were fabricated prior to Sep 2022.

When backgated, devices exhibited *p*-type transistor behaviour with significant hysteresis and negligible gate current leakage. The devices fabricated with a solvent-based deposition were switched off at a lower voltage than the devices which used surfactant during deposition.

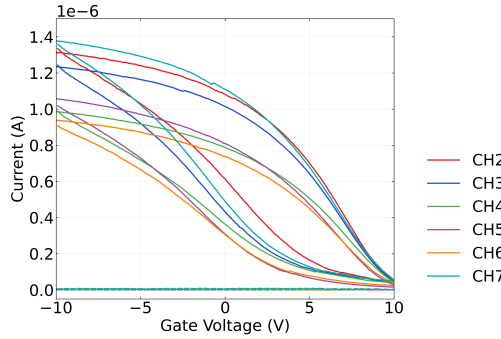
1. Characteristics of Pristine Carbon Nanotube & Graphene Field Effect Transistors



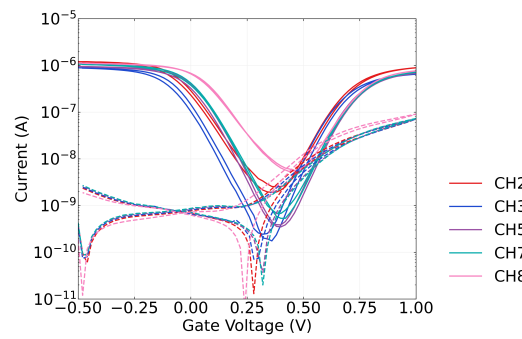
(a) Solvent-based deposition, back-gated



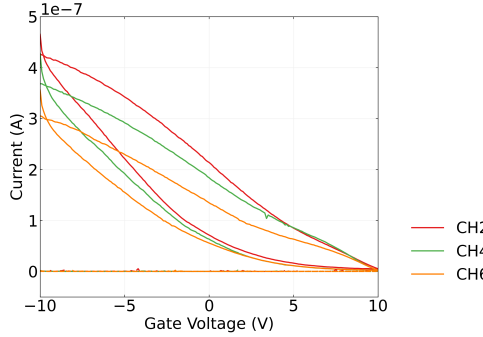
(b) Solvent-based deposition, aqueous-gated



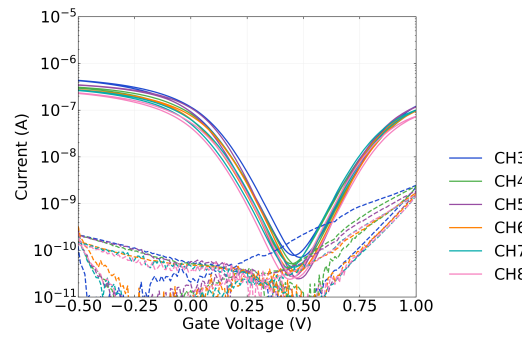
(c) Dropcast surfactant-based deposition, back-gated



(d) Dropcast surfactant-based deposition, aqueous-gated



(e) Steam-assisted dropcast surfactant-based deposition, back-gated



(f) Steam-assisted dropcast surfactant-based deposition, aqueous-gated

Figure 1.3.: Transfer characteristics of carbon nanotube networks deposited using various methods. 1XPBS was used as the buffer for the liquid-gated measurements here. The source-drain voltage used for all sweeps was $V_{ds} = 100\text{mV}$. A step size of 20 mV was used for the liquid-gated sweeps, while a step size of 100 mV was used for the backgated sweeps.

1.3. Salt Concentration Sensing with Phosphate Buffered Saline

When the devices were liquid-gated with 1XPBS electrolyte buffer, they exhibited ambipolar characteristics with significantly less hysteresis than when backgated. When appropriately configured, leakage current across the liquid gate consistently only became significant above $V_g \simeq 0.5$ V. Devices which used carbon nanotube films deposited in surfactant with steam present had significantly less channel-to-channel variation in electrical characteristics than for devices fabricated using other approaches.

Consistent subthreshold regime behaviour between channels is desirable for reliable multiplexed biosensing.

1.3. Salt Concentration Sensing with Phosphate Buffered Saline

-nLOF2020 resist being used leads to devices with less drift!!

A. Photolithography

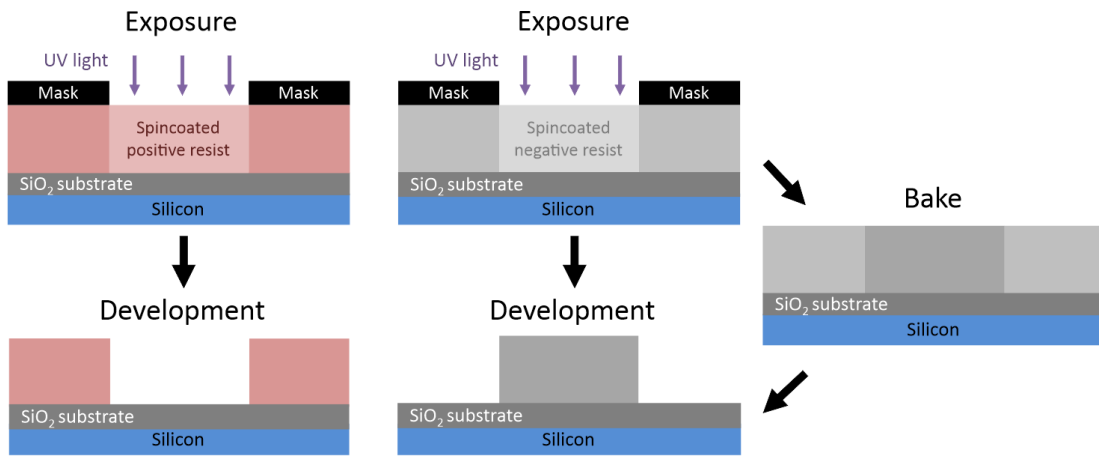


Figure A.1.: A side-view comparison of generic photolithography processes for positive and negative resists in the ideal case. Photolithography with a positive resist requires a single softbake step before exposure, while for negative resists a second baking step is required after exposure (Thicknesses shown not to scale).

This section details some of the standard photolithography procedures used in the device fabrication processes detailed in [?@sec-fabrication](#). Photoresists, also referred to here as “resists”, are UV light-sensitive polymeric resins used for photolithography. Both positive and negative photoresists were used in various fabrication processes. Positive resists are made soluble in alkalines by UV light exposure, meaning exposed areas are removed in the development process. Conversely, negative resists are cross-linked by exposure and a post-exposure bake step. The unexposed areas of the negative resist are then removed in the development process [15]. Figure A.1 gives a visual representation of these differences.

The specific photoresist selected for photolithography depends on the specific use case. The types used in this thesis are positive and negative AZ® photoresists (AZ® 1518, Microchemicals GmbH; AZ® nLOF 2020, Microchemicals GmbH) and SU-8 (SU8-2150, Kayaku Advanced Materials, formerly Microchem). The AZ® resists used here have a minimum film thickness of 1.5 μm [15], while the SU8-2150 has a minimum film thickness of 0.5 μm [16]. Positive resists which have not been thermally crosslinked will soften at higher temperatures ($\gtrsim 100^\circ\text{C}$ for AZ® 1518), leading to a rounded profile. This is not

A. Photolithography

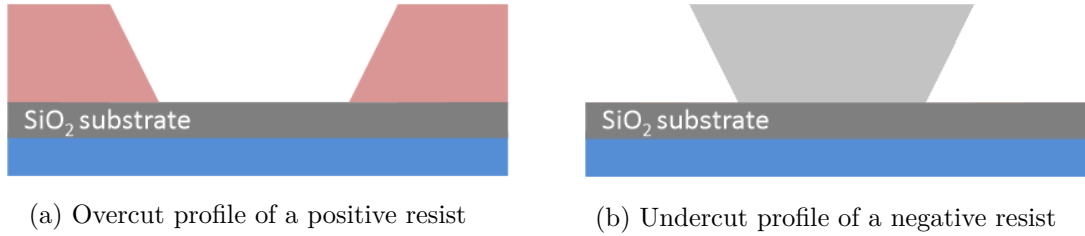


Figure A.2.: Two different resist profiles seen for different types of photoresist. Each profile has had the central region of the substrate exposed to UV light prior to development. The undercut profile is ideal for thin-film metal deposition and subsequent patterned removal, known as “lift-off”.

the case for negative resists, which are more thermally stable [15]. Each resist therefore has a different cross-section profile, as shown in Figure A.2.

If metal deposition is performed on a positive resist, some metal can collect on the outwardly-sloped sidewalls of the resist (see Figure A.2) which forms significant spikes on the edges of the deposited metal upon lift-off. On the other hand, metal cannot collect on top of the inwardly-sloped negative profile sidewalls, which avoids the formation of large edge spikes. Therefore, the negative resist profile is more suited to metal or metal oxide deposition and lift-off processes, though the process is more sensitive to human error due to requiring more processing steps than positive resist [15]. Finally, when it is suitably processed SU-8 is considered to be more stable and biocompatible than other photoresists [17]. It is especially biocompatible when chemically modified via processes such as isopropanol sonication and O₂ plasma treatment [18].

All photolithographic exposure was performed using a Karl Suss MJB3 Contact Aligner with a USHIO super-high pressure 350 W mercury lamp (USH-350DS, Japan). When performing photolithography, the intensity reading from the aligner was 20.8 – 24.2 mW/cm² (Note however that an external photometer reading at 400 nm found an intensity output of 17.2 mW/cm² when the aligner read 21.0 mW/cm²).

In general, photolithography procedures should be performed under yellow lighting, as light wavelengths from 320 – 450 nm can promote reactions in the photoresist used. Aging of photoresist over time can also significantly affect the photolithography process, and therefore all processes should be re-optimised regularly over time to give the desired result [15]. The range in processing times for some steps of the processes used here are largely due to the effects of aging on the photoresist.

The step-by-step processes for each resist are detailed in the subsequent sections.

A.1. AZ® 1518 photoresist

1. Spincoat at a final speed of 4000 rotations per minute (rpm) for 1 minute, with an initial acceleration of 500 rpm/s (notes: clean the substrate with acetone, isopropanol (IPA) and nitrogen before spincoating; use only the minimum amount of photoresist required to fully cover the wafer surface; avoid any gaps or bubbles in the photoresist).
2. Softbake 2 – 4 minutes at 95°C on the hotplate (2 min for individual devices, 4 min for a quarter wafer)
3. Mask expose for 10 – 12 s (note: clean mask with acetone/IPA and N₂ dry before use)
4. Develop with 3 parts AZ® 326 (2.38 % TMAH metal-ion free developer, Microchemicals GmbH) in 1 part deionised (DI) water for 30 – 45 s (note: rinse for 10 – 15 s in one development solution, then perform the rest of the development in clean developer for a cleaner profile; lightly agitate the solution throughout the development process)
5. Rinse device for 30 s in DI water to remove excess developer, then dry under nitrogen

A.2. AZ® nLOF 2020 photoresist

1. Spincoat at final speed of 3000 rotations per minute (rpm) for 1 minute, with an initial acceleration of 500 rpm/s (notes: clean the substrate with acetone, isopropanol (IPA) and nitrogen before spincoating; avoid any gaps or bubbles in the photoresist)
2. Softbake for precisely 60 s at 110°C on the hotplate
3. Mask expose for 2.7 – 3 s (note: clean mask with acetone/IPA and N₂ dry before use)
4. Post-exposure bake for precisely 60 s at 110°C on the hotplate to cross-link exposed resist
5. Develop with 3 parts AZ® 326 in 1 part DI water for 60 – 70 s (note: rinse for 30 s in one development solution, then perform the rest of the development in clean developer for a cleaner profile; lightly agitate the solution throughout the development process)
6. Rinse device for 30 s in DI water to remove excess developer, then dry under nitrogen

A. Photolithography

A.3. SU8-2150 photoresist

1. SU-8 was diluted in cyclopentanone until viscosity was low enough to spincoat on substrate and then sonicated at 50°C for 3 – 4 hours (Note: The dilution ratio used was ~1 part SU-8 to 5 parts cyclopentanone. However, the age of the SU-8 may mean that significant evaporation had occurred prior to use, and the amount of SU-8 actually present is underrepresented by this ratio)
2. Spincoat first with a final speed of 500 rpm (acceleration 500 rpm/s) for 10 seconds, followed by spincoating at 4000 rpm (acceleration 7500 rpm/s) for 40 s.
3. Softbake for 10 minutes at 95°C on the hotplate
4. Mask expose for 6 – 8 s (note: clean mask with acetone/IPA and N₂ dry before use)
5. Post-exposure bake for 10 minutes at 95°C on the hotplate to cross-link exposed resist
6. Develop with SU-8 developer (Kayaku Advanced Materials, formerly Microchem) for 10 – 15 s, then clean in IPA for 30 s, repeat this step once then dry under nitrogen (note: lightly agitate the solution throughout the development process)

B. Python Code for Data Analysis

B.1. Code Repository

The code used for general analysis of field-effect transistor devices in this thesis was written with Python 3.8.8. Contributors to the code used include Erica Cassie, Erica Happe, Marissa Dierkes and Leo Browning. The code is located on GitHub and the research group OneDrive, and is available on request.

B.2. Atomic Force Microscope Histogram Analysis

The purpose of this code is to analyse atomic force microscope (AFM) images of carbon nanotube networks in .xyz format taken using an atomic force microscope and processed in Gwyddion (see [?@sec-afm-characterisation](#)). It was originally designed by Erica Happe in Matlab, and adapted by Marissa Dierkes and myself for use in Python.

$$f(x) = k_1 \exp\left(-\frac{(x - m_1)^2}{2s_1^2}\right) + k_2 \exp\left(-\frac{(x - m_2)^2}{2s_2^2}\right) + \dots \quad (\text{B.1})$$

The .xyz data is initially sorted into bins with 0.15 nm size. The bin with the maximum number of counts is set at 0 nm, as this peak represents the mean of the surface roughness of the bare silicon. The parameters m_i , s_i , k_i ($i = 1, 2, 3$) are used with objective function Equation B.1 to overlay the data with normal distributions. These fitting parameters represent the mean (m), standard deviation (s) and amplitude (k) of each normal distribution. We can make approximations of some of these fitting parameters using the histogram data.

k_1 is taken to be the maximum y-value of the data being fitted, m_1 is set to zero (used as a point of reference) and s_1 is taken as one-third of the difference between m_1 and the x-value of the first datapoint where the y-value is greater than 1% of k_1 (approximating one standard deviation). We find the distribution given by these values using Equation B.1, and subtract it from the existing dataset.

Then, using the analysis technique outlined by Vobornik *et al.* [8] in Gwyddion, we manually find estimates for the mean m_2 and standard deviation s_2 of the carbon nanotube bundle distribution. We then take k_2 to be the maximum y-value of this modified

B. Python Code for Data Analysis

dataset, and m_1 to be the x-value of the maximum y-value. We then set k_2 so that the height of the resulting distribution at one standard deviation matches the height of the .xyz data histogram. We take this distribution, and subtract it from the existing dataset.

The code also allows for discretely binning continuous data from fitted normal distributions and examining the proportion of counts above or below a particular height. 2.9 nm is roughly where 2 bundles with average size 1.45 nm can start to be present, and is used as an estimate of the boundary value between single-tube bundle diameters and multi-tube bundle diameters.

$$f(x) = k_1 \exp\left(-\frac{t}{\tau_1}\right) + k_2 \exp\left(-\frac{t}{\tau_2}\right) + \dots + c \quad (\text{B.2})$$

C. Vapour Delivery System

C.1. Technical Notes

Two LabView Virtual Instruments (VIs) were adapted from pre-existing VIs for operating the mass flow controllers and monitoring vapour flow into the device chamber, as well as monitoring temperature and humidity in the vapour delivery system's manifold. These VIs were named “ ” A third VI was developed in parallel which combined the first two Virtual Instruments, alongside allowing the sequence of values to control the mass flow controllers.

From Honours report: “ ” Figure 12 gives the right side of the front panel of the LabView VI sample with vapour.VI, which lets us preset an autonomously-performed vapour sensing sequence. Each row in each array module corresponds to a different step in this sequence. The ‘howManySteps’ module lets us set how many of these steps are performed. The ‘Durations Array’ module determines the length of time in seconds each step is performed over. The ‘Carrier Flows Array’ and ‘Dilution Flows Array’ modules let us set the carrier flow and dilution flow, respectively, in standard cubic centimetres per minute (sccm) through the gas rig at each step. The carrier flow pushes analyte vapour into the vapour-sensing device chamber, while dilution flow is used to modify the flow behaviour of the analyte vapour entering the chamber. The vapour sensing sequence as depicted in Figure 12 was used for all vapour sensing runs in this investigation. At the end of the sequence, the data collected about the vapour sensing process was saved as an .lvm file. “ ”

C.2. Future Improvements

Bibliography

- [1] H. Y. Zheng and N. O.V. Plank. “Facile fabrication of carbon nanotube network thin film transistors for device platforms”. In: *International Journal of Nanotechnology* 14.1-6 (2017), pp. 505–518. ISSN: 14757435. DOI: 10.1504/IJNT.2017.082473.
- [2] Murugathas Thanihaichelvan, Leo A. Browning, Marissa P. Dierkes, et al. “Data on liquid gated CNT network FETs on flexible substrates”. In: *Data in Brief* 21 (Dec. 2018), pp. 276–283. ISSN: 2352-3409. DOI: 10.1016/J.DIB.2018.09.093.
- [3] Murugathas Thanihaichelvan, Leo A. Browning, Marissa P. Dierkes, et al. “Metallic-semiconducting junctions create sensing hot-spots in carbon nanotube FET aptasensors near percolation”. In: *Biosensors and Bioelectronics* 130 (Apr. 2019), pp. 408–413. ISSN: 0956-5663. DOI: 10.1016/J.BIOS.2018.09.021.
- [4] Hong Phan T. Nguyen, Thanihaichelvan Murugathas, and Natalie O.V. Plank. “Comparison of Duplex and Quadruplex Folding Structure Adenosine Aptamers for Carbon Nanotube Field Effect Transistor Aptasensors”. In: *Nanomaterials (Basel, Switzerland)* 11.9 (Sept. 2021). ISSN: 2079-4991. DOI: 10.3390/NANO11092280. URL: <https://pubmed.ncbi.nlm.nih.gov/34578596/>.
- [5] Wim Wenseleers, Igor L. Vlasov, Etienne Goovaerts, et al. “Efficient Isolation and Solubilization of Pristine Single-Walled Nanotubes in Bile Salt Micelles”. In: *Advanced Functional Materials* 14.11 (Nov. 2004), pp. 1105–1112. ISSN: 1616-3028. DOI: 10.1002/ADFM.200400130. URL: <https://onlinelibrary.wiley.com/doi/full/10.1002/adfm.200400130%20https://onlinelibrary.wiley.com/doi/abs/10.1002/adfm.200400130%20https://onlinelibrary.wiley.com/doi/10.1002/adfm.200400130>.
- [6] Maki Shimizu, Shunjiro Fujii, Takeshi Tanaka, et al. “Effects of surfactants on the electronic transport properties of thin-film transistors of single-wall carbon nanotubes”. In: *Journal of Physical Chemistry C* 117.22 (June 2013), pp. 11744–11749. ISSN: 19327455. DOI: 10.1021/JP3113254/SUPPL_FILE/JP3113254_SI_001.PDF. URL: <https://pubs.acs.org/doi/full/10.1021/jp3113254>.
- [7] Chang Liu and Hui Ming Cheng. “Carbon nanotubes: controlled growth and application”. In: *Materials Today* 16.1-2 (Jan. 2013), pp. 19–28. ISSN: 1369-7021. DOI: 10.1016/J.MATTOD.2013.01.019.
- [8] Dusan Vobornik, Maohui Chen, Shan Zou, et al. “Measuring the Diameter of Single-Wall Carbon Nanotubes Using AFM”. In: *Nanomaterials* 13.3 (Feb. 2023), p. 477. ISSN: 20794991. DOI: 10.3390/NANO13030477/S1. URL: <https://www.mdpi.com/2079-4991/13/3/477/htm%20https://www.mdpi.com/2079-4991/13/3/477>.

Bibliography

- [9] Matěj Velický, Adam J Cooper, Peter S Toth, et al. “Mechanical stability of substrate-bound graphene in contact with aqueous solutions”. In: *2D Materials* 2.2 (May 2015), p. 024011. ISSN: 2053-1583. DOI: 10.1088/2053-1583/2/2/024011. URL: <https://iopscience.iop.org/article/10.1088/2053-1583/2/2/024011%20https://iopscience.iop.org/article/10.1088/2053-1583/2/2/024011/meta>.
- [10] R. L. Graham, B. D. Lubachevsky, K. J. Nurmela, et al. “Dense packings of congruent circles in a circle”. In: *Discrete Mathematics* 181.1-3 (Feb. 1998), pp. 139–154. ISSN: 0012-365X. DOI: 10.1016/S0012-365X(97)00050-2.
- [11] Eckard Specht. *The best known packings of equal circles in a circle*. URL: <http://hydra.nat.uni-magdeburg.de/packing/cci/cci.html> (visited on 2023-09-11).
- [12] Robert D. Deegan, Olgica Bakajin, Todd F. Dupont, et al. “Capillary flow as the cause of ring stains from dried liquid drops”. In: *Nature* 1997 389:6653 389.6653 (1997), pp. 827–829. ISSN: 1476-4687. DOI: 10.1038/39827. URL: <https://www.nature.com/articles/39827>.
- [13] R. T. van Gaalen, C. Diddens, H. M.A. Wijshoff, et al. “Marangoni circulation in evaporating droplets in the presence of soluble surfactants”. In: *Journal of Colloid and Interface Science* 584 (Feb. 2021), pp. 622–633. ISSN: 0021-9797. DOI: 10.1016/J.JCIS.2020.10.057.
- [14] Mindy D. Bishop, Gage Hills, Tathagata Srimani, et al. “Fabrication of carbon nanotube field-effect transistors in commercial silicon manufacturing facilities”. In: *Nature Electronics* 2020 3:8 3.8 (June 2020), pp. 492–501. ISSN: 2520-1131. DOI: 10.1038/s41928-020-0419-7. URL: <https://www.nature.com/articles/s41928-020-0419-7>.
- [15] MicroChemicals. *Photoresists AZ and MicroChemicals TI resists*. URL: <https://www.microchemicals.com/products/photoresists.html> (visited on 2023-06-09).
- [16] Kayaku (Microchem). *SU-8 2000 Permanent Negative Epoxy Photoresist / Kayaku*. URL: <https://kayakuam.com/products/su-8-2000/> (visited on 2023-06-30).
- [17] Faris M. Albarghouthi, Nicholas X. Williams, James L. Doherty, et al. “Passivation Strategies for Enhancing Solution-Gated Carbon Nanotube Field-Effect Transistor Biosensing Performance and Stability in Ionic Solutions”. In: *ACS Applied Nano Materials* 5.10 (Oct. 2022), pp. 15865–15874. ISSN: 25740970. DOI: 10.1021/ACS/ANM.2C04098/SUPPL_FILE/AN2C04098_SI_001.PDF. URL: <https://doi.org/10.1021/acsanm.2c04098>.
- [18] Ziyu Chen and Jeong Bong Lee. “Biocompatibility of SU-8 and Its Biomedical Device Applications”. In: *Micromachines* 2021, Vol. 12, Page 794 12.7 (July 2021), p. 794. ISSN: 2072-666X. DOI: 10.3390/MI12070794. URL: <https://www.mdpi.com/2072-666X/12/7/794>.